LANGMUIR

pubs.acs.org/Langmuir Article

Numerical Simulation Analysis of Two-Terminal Monolithic Perovskite-CIGS Tandem Solar Cell for Enhanced Photovoltaic Performance Using SCAPS-1d

Alok Kumar, Sushama M. Giripunje,* Mukesh Bharadwaj, and Deboraj Muchahary

Cite This: *Langmuir* 2025, 41, 19729−19741 Read Online

ACCESS | Metrics & More | Article Recommendations

ABSTRACT: This research designs and simulates a high-efficiency tandem solar cell (TSC) using SCAPS-1D (3.3.12), exploiting tandem perovskite technology for enhanced performance. The agenda of our work is here to minimize the two largest losses associated with single-junction solar cells like thermalization and transmission losses by absorbing a broader spectrum of sunlight using $CsGeI_3$/CIGS tandem solar cell technology. To ensure the accuracy of the simulated results, the authors first calibrate both the top and bottom solar cells using experimental data and compare the simulated results with experimental findings. This study investigates the impact of thickness, parasitic resistance, temperature, quantum efficiency, band diagram, absorption coefficients, and two-diode model equivalent circuit parameters on solar cell performance. This work optimizes lead-free, wide bandgap (1.6 eV) $CsGeI_3$ perovskite and narrow bandgap (1.1 eV) CIGS solar cells individually and then proposes a tandem solar cell structure using a filtered spectrum approach. The proposed $CsGeI_3$/CIGS tandem solar cell device structure is studied in detail and simulated using SCAPS 1D. A tandem configuration, with a thickness of a 273 nm top cell (simulated under AM1.5G) and a 1000 nm bottom cell, achieved conversion efficiencies of 16.93% and 16.49%, respectively, with respective J_{SC} values of 19.31 mA cm^{-2}/19.32 mA cm^{-2}. By adding the voltages at same current points to make the tandem J-V curve, this design yielded a 26.06% efficient perovskite-CIGS tandem cell with V_{OC} of 1.73 V, J_{SC} of 19.32 mA cm^{-2}, and FF of 77.98%. This perovskite-CIGS tandem design demonstrates a promising route for developing high-efficiency, low-cost TSCs.

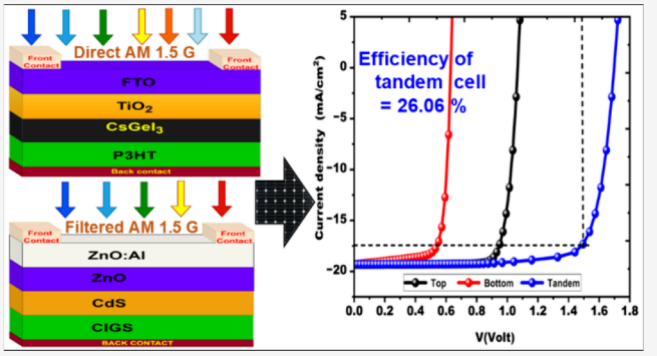

1. INTRODUCTION

Perovskite-based tandem solar cells hold promise as a cost-effective photovoltaic technology due to their potential for high power conversion efficiency (PCE) through the optimized utilization of the solar spectrum.[1] Silicon, CIGS, and low-bandgap perovskite are promising bottom cell materials for efficient tandem solar cells to meet increasing energy demands.[2] The world faces a significant challenge in meeting growing energy demands.[3] Global energy consumption is projected to rise from 472 Quads in 2006 to 678 Quads in 2030, representing an average annual increase of 1.8%.[4] Harvesting just 0.02% of solar energy reaching earth would meet our energy needs.[5] Currently, the energy requirement is mainly fulfilled by fossil fuels followed by renewable sources of energy such as wind, hydro, and solar.[6] Solar power offers a promising avenue for safe and sustainable energy, and tandem solar cells can help overcome the efficiency limitations of photovoltaic modules.[1] Researchers are extensively investigating semiconductor materials to develop efficient, cost-effective, and long-lasting solar cells (SCs). Currently, various single-junction c-Si cells[7,8] command over 90% of global solar production. Silicon solar cells exceed 26% power conversion efficiency.[9] Silicon solar cells, while dominant, suffer from complex fabrication, rigidity, limited light absorption, and poor flexibility (<30 degrees), driving the search for alternative materials and suggested designs to enhance performance and sustainability. Single-junction (1N) SCs are limited to a maximum efficiency of 33% according to the Shockley and Quessier (S-Q) limit.[10] A pictorial representation of lattice thermalization losses and nonabsorbed photon losses is shown in Figure 1a, and these losses are the primary reasons not to conquer the SQ limit by single-junction solar cells.[11] To minimize these losses and efficiently utilize the maximum

Received: March 28, 2025
Revised: July 11, 2025
Accepted: July 14, 2025
Published: July 23, 2025

https://doi.org/10.1021/acs.langmuir.5c01551
Langmuir 2025, 41, 19729−19741

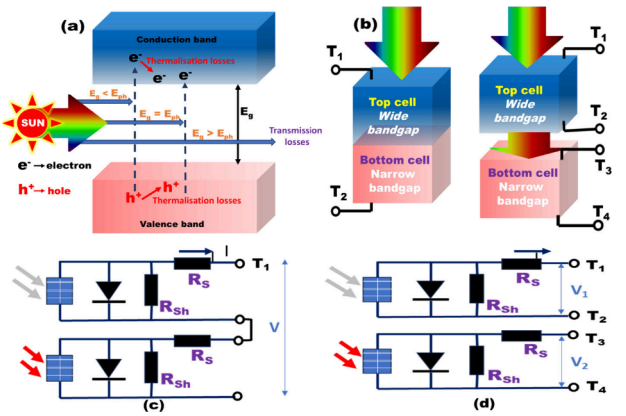

Figure 1. (a) Power loss diagram for single-junction solar cells, including thermalization and transmission losses; (b) 2-T (left) and 4-T (right) architectures for perovskite/CIGS tandem solar cells; (c) Equivalent circuit of 2-T tandem cell; (d) Equivalent circuit of 4-T tandem cell.

spectrum, both wide and narrow bandgap materials are utilized for designing top and bottom solar cells that open the door for tandem solar cell technology; this idea was presented by Jackson in 1955.[12] Tandem cells were designed by using wide bandgap top cells (1.5−1.9 eV) and narrow bandgap bottom cells (0.9−1.3 eV) to absorb a wider range of the light spectrum. This design allows effective absorption of high-energy photons by the top cell, diminishing thermalization losses and producing a high voltage. Concurrently, the bottom cell traps low-energy photons shown in Figure 1b that penetrate through improving the overall utilization of the solar spectrum.[13] The two most common tandem architectures are mechanically stacked four-terminal (4 T) tandem and two-terminal (2 T) monolithic structures, as shown in Figure 1b, and equivalent circuits of 2-T and 4-T perovskite/CIGS tandem solar cells shown in Figure 1c,d. The 2T monolithic structure connects solar cells in series by matching their current densities, minimizing power loss through interconnection layers and treating the device as a single unit. In 1980, Lamort et al. developed a series-connected dual-junction photovoltaic cell.[14] Kim et al. achieved a record 19.8% efficiency for CIGS/Si tandem cells.[15] Mousa et al. achieved 30.52% efficiency with $MaPbI_3$/CIGS tandem solar cells in 2021.[16] Top cells can utilize both inorganic and organic materials with a wide bandgap. Inorganic materials like CdTe, Si, CIGS, and GaAs are potential candidates that offer excellent mobility and absorption coefficient and exceptional radiation resistance.[17] Tandem architectures offer a promising route to improve solar cell efficiency, with several configurations like perovskite/silicon,[18,19] perovskite/CIGS,[2,20] and perovskite/perovskite[21−25] tandems along with all quantum dot solar cell structures.[26,27] Perovskites exhibit strong light absorption and simple solution-based fabrication, leading to rapid efficiency gains from 3.8% in 2009 to 25.70% in 2024.[28] Perovskites are well-suited for tandem solar cells due to their excellent photoelectric properties, tunable band gaps, mechanical durability, low cost, and solution-based fabrication.[29] Researchers have identified metal halide perovskites (ABX_3), which absorb light in the visible spectrum, for potential application in photovoltaic technology, and later they are named after the Russian mineralogist L. A. Perovski. Cesium (Cs), methylammonium (MA), and formamidinium (FA) are typically denoted as A (monovalent cation), with Pb or Sn as B (divalent cation), and I, Br, or Cl as X (halide anion). Perovskites are a strong candidate for photovoltaics due to their low cost, variable bandgap (1.1−2.3 eV), good carrier mobility ($\mu_e \sim 5-10$ cm^2 V^{-1} s^{-1} and $\mu_h \sim 1-5$ cm^2 V^{-1} s^{-1}), and long carrier lifetime (~1 μs).[30] Perovskite tandem solar cells, first appearing in 2014 with approximately 14% conversion efficiency, have since achieved efficiencies exceeding 25% (Werner et al.), 23.6% (Bush et al.), and 25.2% (Sahli et al.).[21] Among these, perovskite/CIGS TSCs have demonstrated substantial compensations in bandgap tunability, versatility, and durability.[31] In this work, the authors focus on lead-free perovskite/CIGS tandem solar cells. CIGS is a well-established light absorber for PV cells due to its optimal bandgap, high absorption coefficient (up to 10^7 m^{-1}), and excellent stability.[32] CIGS is highly suitable for designing tandem solar cells as it offers a tunable bandgap ranging from 1.04 to 1.69 eV by adjusting the gallium (Ga) content in the CIGS material.[33] In this work, after detailed investigations, lead-free $CsGeI_3$ perovskite with a bandgap of 1.6 eV is found suitable for perovskite/CIGS tandem solar cell.[34−42] Its high absorption coefficient enables efficient light harvesting and enhanced carrier generation and transport. Chen et al. first fabricated lead-free $CsGeI_3$ halide perovskite via a simple solvothermal route, achieving a power conversion efficiency of approximately 4.92% under an AM of 1.5 G after tuning the $CsGeI_3$ quantum rod configuration. $CsGeI_3$, a lead-free and novel perovskite material, requires consideration of its environmental stability over long-term usage, particularly under high-temperature and high-humidity conditions. Krishnamoorthy et al.'s computational and experimental results on $CsGeI_3$ suggest germanium as a suitable lead substitute in halide perovskites for solar cells. Their experimental photocurrent results of approximately 5.7 mA/cm^2 confirm the durable potential of Ge-based lead-free halide perovskite compounds in photovoltaic applications.[43] CIGS, a mature thin-film material, is well-suited for solar cells due to its broad light absorption, efficient charge transport, and high stability. CIGS is a highly efficient thin-film semiconductor used in photovoltaics because of its direct bandgap and strong light absorption. The bandgap, tunable from 1.0 to 1.7 eV by adjusting the Ga/In ratio, optimizes spectral utilization for tandem applications. Low defect density and high carrier mobility ensure superior charge transport, boosting the power conversion efficiency. Interface engineering and doping strategies improve junction properties, minimizing recombination losses and enhancing stability. CIGS solar cells, achieving efficiencies over 23%, are a competitive alternative to silicon photovoltaics.[44] CIGS solar cells offer advantages over silicon due to their thin-film construction, resulting in lighter weight and greater flexibility. Furthermore, CIGS exhibits a lower temperature coefficient, maintaining higher efficiency in hot climates compared to silicon.[45] Perovskite and CIGS thin-film solar cells offer flexible, lightweight devices with high power-to-weight ratios, making them well-suited for space applications.[46,47] This study focuses on materials with a high technological potential and significant field impact. They were selected for their sustainability and promising manufacturability in next-generation photovoltaics. This study seeks a cost-effective and stable lead-free perovskite material to improve the efficiency of perovskite/CIGS tandem solar cells. All perovskite-CIGS TSCs are an emerging PV technology for high-efficiency SCs. The primary goal of this study is to

https://doi.org/10.1021/acs.langmuir.5c01551
Langmuir 2025, 41, 19729−19741

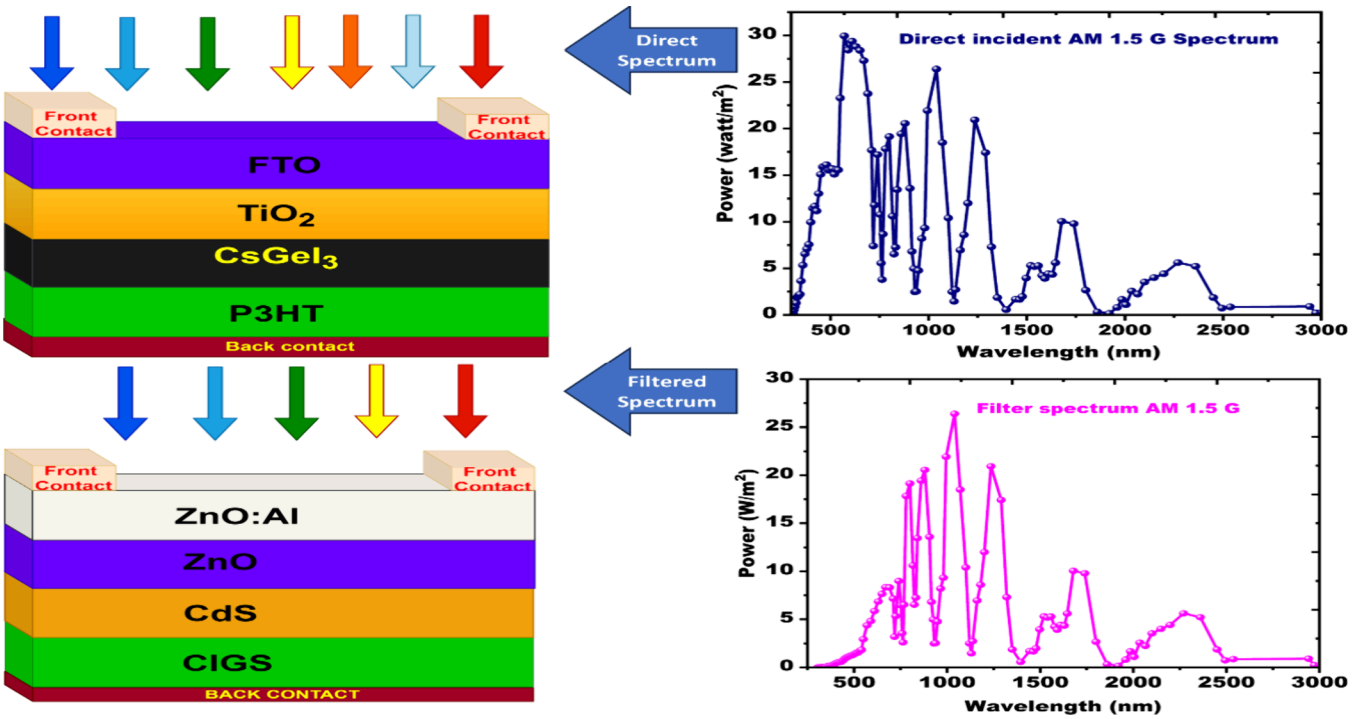

Figure 2. Tandem solar cell architectures using direct and filtered AM 1.5G spectrum.

optimize the device parameters of an environmentally friendly $CsGeI_3$/CIGS tandem solar cell to maximize its performance, positioning it as a potential alternative to lead-based counterparts. This is achieved by tuning the thicknesses of the top and bottom cells to ensure current matching, thereby improving the overall efficiency by reducing thermalization and transmission losses typical in single-junction solar cells. Furthermore, the choice of a perovskite/CIGS tandem structure over the conventional perovskite/silicon tandem is primarily motivated by its lightweight nature and compatibility with flexible substrates. In existing research, lead (Pb), a hazardous substance, was employed in the top cells of perovskite solar cells.[48] Given lead's mutagenic toxicity and associated health risks, a lead-free tandem solar cell structure is proposed after detailed investigation.[49] The proposed perovskite/CIGS tandem solar cell offers a 26.06% conversion efficiency. Tandem cell research advances solar energy by increasing efficiency and exploring innovative materials and designs. These improvements lead to more cost-effective PV cells, reduce recombination, and accelerate the adoption of sustainable energy sources.

2. MATERIALS AND METHODS

Employing simulation and modeling in semiconductor device design saves time and resources by enabling researchers to validate theoretical computations prior to fabrication.[50] The $CsGeI_3$/CIGS tandem solar cell simulation is conducted using SCAPS-1D, a widely used powerful tool among photovoltaic researchers worldwide that accommodates extensive variations in material input parameters, yielding realistic results closely aligned with experimental data.[51−54] The fundamental equations guiding this simulation are continuity (eq 1), current densities of electron and holes given by equations (eqs 2 and 3) and Poisson's equation (eq 8), along with some other supporting equations for free charge carriers given by the following equations.[55]

Continuity equations for an electron and holes:

$$\frac{\partial j_n}{\partial x} + G_n(x) - R_n(x) = 0 \quad \text{and} \quad \frac{\partial j_p}{\partial x} - G_p(x) + R_p(x) = 0 \tag{1}$$

The corresponding current densities of electron and holes are given by eqs 2 and 3.

$$J_n = q\left(D_n \frac{\mathrm{d}n}{\mathrm{d}x} + \mu_n n \frac{\mathrm{d}\varnothing}{\mathrm{d}x}\right) \tag{2}$$

$$J_p = -q\left(D_p \frac{\mathrm{d}p}{\mathrm{d}x} - \mu_p p \frac{\mathrm{d}\varnothing}{\mathrm{d}x}\right) \tag{3}$$

Diffusion length and diffusivity describe how far and how fast charge carriers (electrons and holes) move before recombining. They are given by an equation (eqs 4 and 5).

$$\text{Diffusion length: } L_{n,p} = \sqrt{D_{n,p}\tau_{n,p}} \tag{4}$$

$$\text{Diffusivity: } D_{n,p} = \left[\left(\frac{k_B T}{q}\right)\mu_{n,p}\right] \tag{5}$$

The open-circuit voltage of the solar cell when no current is drawn is given by eq 6. The carrier lifetime, i.e., the average time of a photogenerated carrier existing before recombining, is given by eq 7.

$$\text{Open circuit voltage: } V_{OC} = \left(\frac{nk_B T}{e}\right)\left[\ln\left(\frac{I_L}{I_0} + 1\right)\right] \tag{6}$$

$$\text{Carrier lifetime: } \tau = \frac{1}{\sigma N_t V_{th}} \tag{7}$$

$$\text{Poisson's equation: } \frac{\mathrm{d}^2}{\mathrm{d}x^2}V(x) = \frac{q}{\varepsilon_0 \varepsilon_r}[p(x) - n(x) + N_D - N_A + \rho_p - \rho_n] \tag{8}$$

The electrostatic potential is V(x), and the electron charge is q. Vacuum and relative permittivity are ε_0 and ε_r, respectively. Donor and acceptor densities are N_D and N_A, while hole and electron

https://doi.org/10.1021/acs.langmuir.5c01551
Langmuir 2025, 41, 19729−19741

Table 1. SCAPS Input Parameter for Various Layers of Top and Bottom Solar Cells Adopted from the Literature[35,56−58]

	Top cell				Bottom Cell			
Material Properties	$CsGeI_3$	P3HT	TiO_2	FTO	CIGS	CdS	ZnO	ZnO:Al
Thickness (nm)	273	40	40	50	1000	45	50	100
Bandgap (eV)	1.6	2.0	3.2	3.5	1.1	2.4	3.3	3.6
Electron affinity (eV)	3.52	3.2	3.9	4.0	4.31	4.2	4.4	4.4
Dielectric permittivity (ε_r)	18.0	4.2	9.0	9.0	13.6	10	9.0	9.0
CB effective DOS N_C (cm^{-3})	1.0×10^{18}	2.0×10^{21}	2.0×10^{18}	2.0×10^{18}	2.2×10^{18}	2.2×10^{18}	2.2×10^{18}	1.0×10^{18}
VB effective DOS N_V (cm^{-3})	1.0×10^{19}	2.0×10^{21}	1.8×10^{19}	1.8×10^{19}	1.8×10^{19}	1.8×10^{19}	1.8×10^{18}	1.0×10^{19}
Electron mobility μ_n ($cm^2\ V\ s^{-1}$)	20	1.8×10^{-3}	100	20	100	100	100	100
Hole mobility μ_p ($cm^2\ V\ s^{-1}$)	20	1.8×10^{-3}	25	10	25	25	25	30
Donor density, N_D (cm^{-3})	0	0	1.0×10^{16}	1.0×10^{15}	0	1.0×10^{18}	1.0×10^{18}	1.0×10^{19}
Acceptor Density N_A (cm^{-3})	2.0×10^{16}	1.0×10^{19}	0	0	9.0×10^{16}	0	0	0
N_t (cm^{-3})	1.0×10^{15}	1.0×10^{15}	1.0×10^{15}	1.0×10^{15}	1.0×10^{14}	1.0×10^{18}	1.0×10^{17}	1.0×10^{17}
Interfacial parameters								
Interface	N_t (cm^{-2})	Defect Energy level E_t (eV)	Defect type		Capture Cross Section of electrons/holes (cm^2)			
P3HT/CsGeI3	1.0×10^{12}	0.6 eV	Neutral		1.0×10^{-19}			
$CsGe_3/TiO_2$	1.0×10^{12}	0.6 eV	Neutral		1.0×10^{-19}			
TiO_2/FTO	1.0×10^{12}	0.6 eV	Neutral		1.0×10^{-18}			
CIGS/CdS	1.0×10^{10}	0.6 eV	Neutral		1.0×10^{-19}			
CdS/ZnO	1.0×10^{10}	0.6 eV	Neutral		1.0×10^{-19}			
ZnO/ZnO:Al	1.0×10^{11}	0.6 eV	Neutral		1.0×10^{-18}			

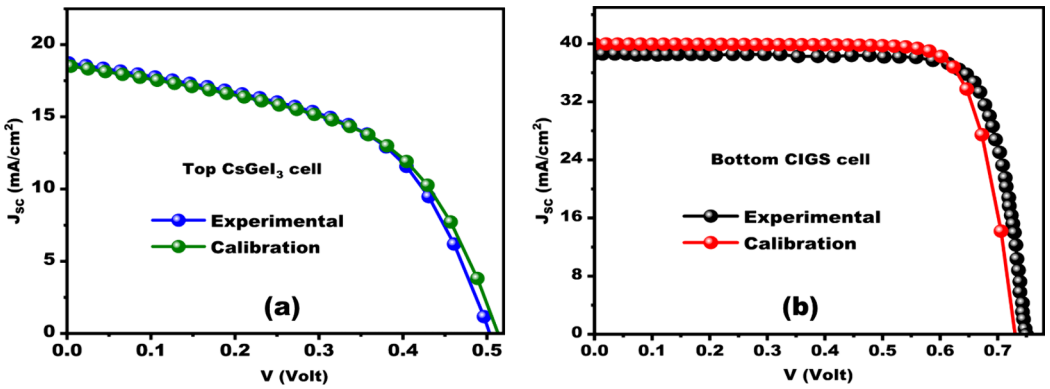

Figure 3. Calibration of (a) $CsGeI_3$ and (b) CIGS solar cells with experimental data to validate the simulated results.

distributions are ρ_p and ρ_n. The recombination rate is R, and hole and electron current densities are J_p and J_n. Electron and hole diffusion constants are D_n and D_p. Carrier generation rate is G, electron and hole mobilities are μ_n and μ_p, and electron and hole lifetimes are $\tau_{n,p}$. Thermal voltage is k B T/e, light-generated current is I_L, saturation current is I_0, capture cross-section is σ, and total defect density is N_t. The tandem solar cell PCE is calculated from J_{SC}, V_{OC}, FF, and incident power P_{in} from the equations (eqs 9 and 10).

$$PCE(\eta) = \frac{V_{oc} \times J_{sc} \times FF}{P_{in}} \tag{9}$$

$$FF = \frac{V_{max} \times J_{max}}{V_{OC} \times J_{SC}} \tag{10}$$

In Figure 2 the top and bottom solar cells (in the left side) are illuminated by direct incident and filtered AM 1.5G light spectrum (in the right side). The configuration is optimized to achieve its highest performance. The modified top cell includes a wide-bandgap lead-free perovskite $CsGeI_3$ absorber layer with a bandgap of 1.6 eV, flanked by P3HT as the hole transport layer (HTL) and TiO_2 as the electron transport layer (ETL).[35,38,39] Fluorine-doped tin oxide (FTO) serves as the transparent conducting layer for the front contact. The bottom CIGS cell has a 1.1 eV bandgap, absorbing light in the near- and far-infrared regions.[44,59] Aluminum and nickel are utilized for the front and back contacts for top and bottom solar cells, respectively. The material parameters employed for simulating the top and bottom cells are summarized in Table 1. The simulation accounts for interface defect densities at both the HTL/perovskite and ETL/perovskite interfaces with a total defect density of approximately 10^{12} cm^{-2}. Additionally, defects are positioned at 0.6 eV above the valence band maximum (VBM) in the energy band structure. The top cell is exposed to the AM 1.5G solar spectrum, while the bottom CIGS cell receives the filtered spectrum transmitted from the top cell calculated with help of the following equations (eqs 11 and 12).[60]

$$S_{Ft}(\lambda) = S_{in}(\lambda) \times \exp\left\{ \sum_{k=1}^{4} - (\alpha_{mat_k}(\lambda) \times d_{mat_k}) \right\} \tag{11}$$

where absorption coefficient (α) is given by

$$\alpha_{mat_k}(\lambda) = \left(\alpha_0 + \beta_0 \frac{E_G}{h\nu}\right)\sqrt{\left(\frac{h\nu}{E_g} - 1\right)} \tag{12}$$

In eq 11 S_{Ft} (λ) is the transmitted filtered spectrum, and S_{in} (λ) is the AM 1.5 direct incident spectrum; α represents absorption coefficient of material, and d_{mat} indicates the thickness of the specific material (mat_k = 1, 2, 3, and 4 for FTO, TiO_2, $CsGeI_3$, and P3HT, respectively). The absorption coefficient of each layer of the top cell is taken from the SCAPS database. The SCAPS database calculates the absorption coefficient with the help of eq 12, where $\alpha_0 = 10^3/m$, β_0 =

https://doi.org/10.1021/acs.langmuir.5c01551
Langmuir 2025, 41, 19729−19741

10^{10}/m, E_g is the bandgap of the material, h is Planck's constant, and ν is the frequency of incident light.

2.1. Calibration of Simulated Data with Experimental Works for Validation. Before an in-depth analysis of the proposed tandem solar cell (TSC), the simulated results were validated through reported experimental data for $CsGeI_3$-based PSCs and CIGS-based single-junction SCs. The top $CsGeI_3$ cell was initially calibrated to match experimental values, which reported a relatively low power conversion efficiency (PCE) of 4.94%, with J_{SC} of 18.11 mA/cm^2, V_{OC} of 0.51 V, and a fill factor (FF) of 53.1% as depicted in Figure 3a.[61] The calibrated results are also shown in Table 2. Upon achieving consistency with experimental results, the cell structure was modified by introducing a P3HT hole transport layer (HTL) to enhance the device performance. This approach to simulation calibration is consistent with prior studies.[35,43] The P3HT is selected due to its lower cost and superior ambient stability compared to Spiro-OMeTAD, which typically requires unstable dopants such as Li-TFSI and tBP that negatively affect device longevity. Moreover, P3HT exhibits favorable energy-level alignment with $CsGeI_3$, promoting efficient hole extraction and reducing recombination losses.[62,63] In contrast, the bottom CIGS cell, calibrated with a thickness of 1000 μm under direct AM 1.5 G spectrum, exhibited a PCE of 23.10% under AM 1.5 G illumination, closely aligning with the experimentally reported value of 22.92% as shown in Figure 3b.[64] After successful calibration of standalone solar cells, a filtered spectrum representative of light transmitted through the top cell was applied to the bottom cell, and simulation results were extracted. This methodology of calibrating simulations based on experimental data is well-supported in the literature.[65−67]

Table 2. Calibration of the Cells and Comparison of Simulated Data with Experimental Findings

Parameters	Experimental measurement (Under Direct illumination of AM1.5 G spectrum)	CalibratedCell (Under Direct illumination of AM1.5 G spectrum)	Optimized Simulation (Top and bottom cell illuminated by Direct and Filtered AM 1.5 spectrum, respectively)
		Top $CsGeI_3$ solar cell	
V_{OC}	0.51	0.52	1.06
J_{SC}	18.11	18.54	19.32
FF	53.1	52.06	82.04
η	4.94	4.96	16.93
		Bottom CIGS solar cell	
V_{OC}	0.74	0.73	0.61
J_{SC}	38.50	39.98	19.31
FF	79.70	78.78	76.72
η	22.92	23.10	16.49

Calibration aligns simulation parameters with real-world conditions, minimizing performance prediction errors. Comparing simulated data to experimental results validates model accuracy, refines assumptions, and improves reliability. This iterative process enhances simulation credibility, enabling advancements in research and technology. Comparative analysis of calibrated parameters with experimental findings is presented in Table 2, while the J-V characteristics of both simulated and experimental $CsGeI_3$ and CIGS cells, shown in Figure 3a,b, confirm a strong correlation between simulated predictions and experimental data.[43]

3. BAND DIAGRAM ANALYSIS OF THE TOP AND BOTTOM SOLAR CELL

Energy band diagrams (EBDs) of top and bottom subcells are very helpful to understand the charge carrier dynamics and band alignment of the PV performance of the device.[68] Space charge region or depletion region refers to a nonzero charge density region while a quasi neutral region has zero charge density region. Energy band alignment of the different layers utilized in the simulation is illustrated in Figure 4a,b, and this represents the electron affinity, energy of the valence band maxima, conduction band minima, and work function of the electrodes. When light shines on the solar cells, electron−hole pairs are generated and indicated by black and red colors, respectively, in Figure 4a,b. To separate these charge carriers for current flow, asymmetry in the semiconductor device is required, and $P-N$ junction has such asymmetry which provides a built-in electric field at the junction.[69]

Under AM1.5G illumination at 300 K of the top solar cells, electron−hole pairs are generated in the SC's absorber layer and pass through the ETL and HTL to be collected at the contacts. The small conduction band offset (−0.38 eV) at the $TiO_2/CsGeI_3$ interface facilitates electron flow from the absorber to the FTO via TiO_2. Conversely, the large valence band offset at the same interface hinders the hole flow to FTO. The higher conduction band offset between P3HT and $CsGeI_3$ blocks electron flow from the absorber to the contact. However, the P3HT's higher valence band energy level enables efficient hole extraction and transport. Furthermore, the ETL/absorber and absorber/HTL interfaces establish a strong electric field that promotes charge carrier separation and collection while impeding the flow of carriers with opposite charges.[70] In the bottom CIGS cell, filtered AM 1.5G light creates electron−hole pairs. The electric field at the CdS/CIGS interface separates these pairs, driving electrons to the ZnO:Al layer and holes to the CIGS layer for collection at the respective contacts.[71]

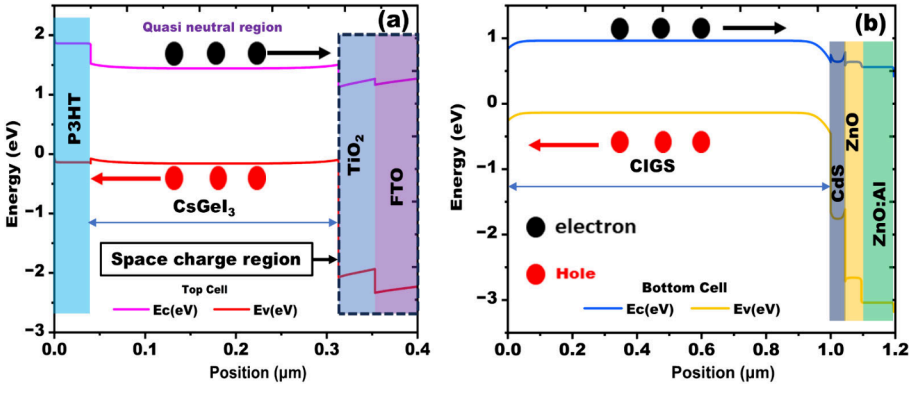

Figure 4. Standalone energy band diagrams of (a) P3HT/$CsGeI_3$/TiO_2/FTO and (b) CIGS/CdS/ZnO/ZnO:Al.

https://doi.org/10.1021/acs.langmuir.5c01551
Langmuir 2025, 41, 19729−19741

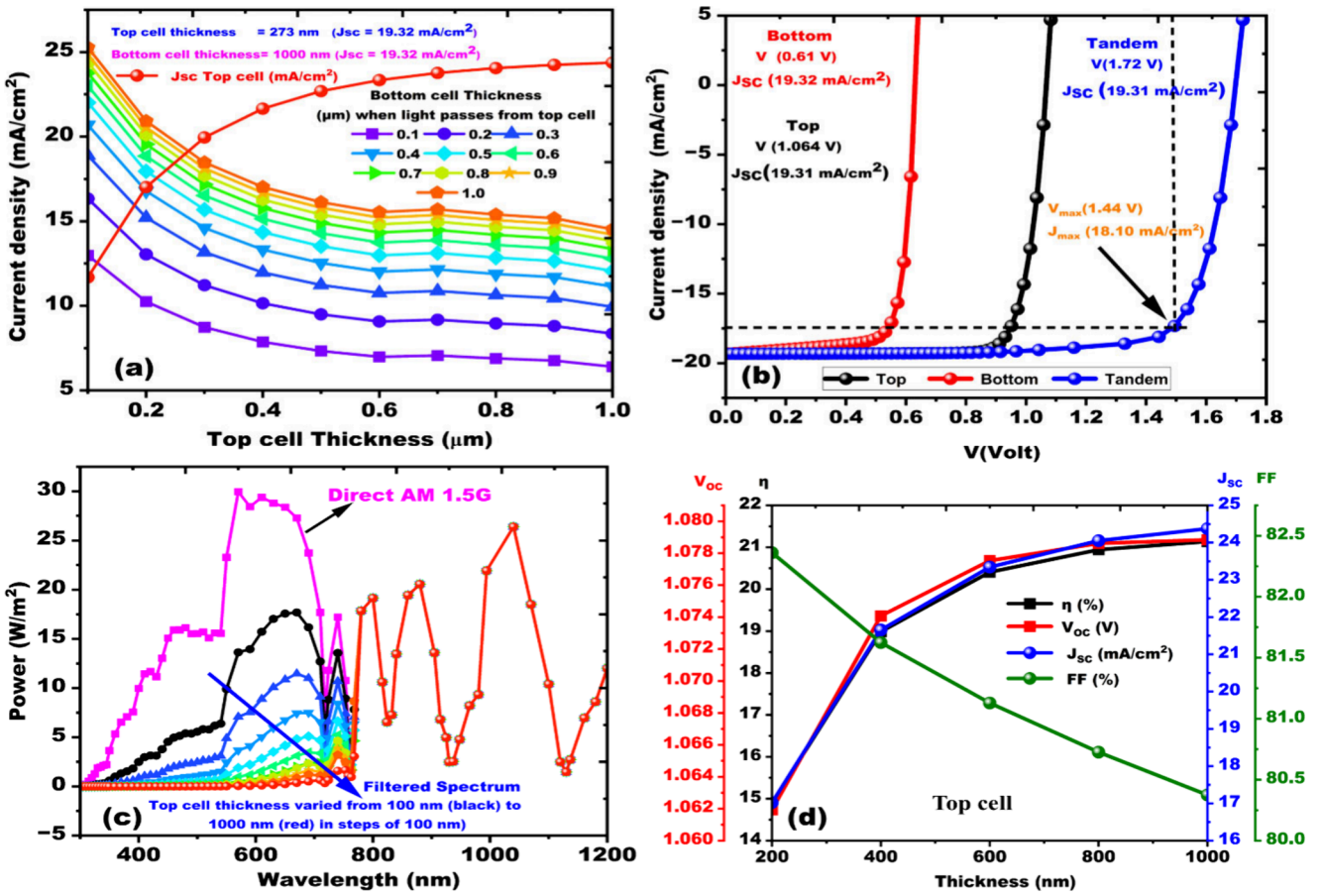

Figure 5. (a) Thickness variation of bottom solar cell from 0.1 to 1 μm under filter spectrum to match J_{SC} of the top solar cell. (b) JV curve analysis of top, bottom, and TSC. (c) Filtered spectrum by changing the thickness of top solar cell absorber material shown by black to red graph and direct spectrum shown by pink color. (d) Impact of top cell absorber thickness on PV parameters.

4. RESULTS AND DISCUSSION

4.1. JV Curve Analysis and Impact of Thickness on PV Parameters. JV (current density−voltage) curves are essential for evaluating tandem solar cell performance, which arises from their stacked subcells' ability to absorb a broader solar spectrum. Analyzing the J-V curve allows researchers to optimize subcell materials, thicknesses, and bandgaps for improved current matching and higher efficiency. Figure 5a shows the current matching of both the top and bottom solar cell for making the 2T tandem device of CIGS and perovskite solar cells. As the thickness of the top and bottom cell increases from 0.1 to 1.0 μm, then the J_{SC} starts to increase due to enhanced photon absorption and charge carrier generation. However, excessive thickness leads to increased recombination losses and series resistance, ultimately limiting the device performance. Mismatched currents cause energy losses and lower efficiency. The top and bottom cell absorber material thickness changes from 0.1 to 1.0 μm under direct and filtered AM 1.5G spectrum as shown in Figure 5c, respectively. The maximum current matching condition is obtained at the optimized top and bottom solar cell thicknesses of 273 and 1000 nm, respectively. Current matching ensures equal contribution from both subcells, maximizing power production by balancing band gaps, thicknesses, and materials. Once the current matching condition is obtained, we make the two terminal tandem devices. Mismatched currents lead to energy losses, as the overall current is constrained by the weaker subcells. Therefore, matching currents is crucial for a high-efficiency TSC. In 2T tandem configuration the maximum power is given by eq 13.[55]

$$P_{\max} = (J_{MPP} \times V_{MPP}) \tag{13}$$

J_{MPP} and V_{MPP} represent the current density and voltage at the maximum power point (MPP) of the TSC. The calculated values of the PV parameters from equations (eqs 9 and 10) of Top, Bottom, and TSCs are tabulated in Table 2. Figure 5b shows the individual J-V characteristics of top, bottom, and tandem solar cell with V_{OC} of 1.06 0.61, and 1.73 V respectively. The J-V curves of the top subcells (measured under AM1.5G) and the bottom subcells (measured under a filtered spectrum) were distinctly obtained and combined in series at equal current. This approach ensures that the voltages are summed while maintaining current continuity, yielding the tandem J-V characteristics. The resulting tandem design demonstrates a remarkable conversion efficiency of 26.06%, a V_{OC} of 1.73 V, a J_{SC} of 19.32 mA/cm^2, and a FF of 77.98%, highlighting its potential for high-performance photovoltaic applications.

Table 3 shows that the top and bottom solar cells have photoconversion efficiencies of 16.93% and 16.49%, respectively. The higher J_{SC} observed in Table 3 likely results from the tandem structure's improved optical and electrical design. This includes enhanced light absorption from optimized layer thicknesses, reduced recombination losses at interfaces, and efficient charge extraction. Improved band alignment between

https://doi.org/10.1021/acs.langmuir.5c01551
Langmuir 2025, 41, 19729−19741

Table 3. PV Parameters of Top, Bottom, and TSCs

PV Parameters	V_{OC} (V)	J_{SC} (mA/cm^2)	FF (%)	PCE (%)
Top	1.06	19.31	82.04	16.93
Bottom	0.61	19.32	76.72	16.49
Tandem	1.73	19.32	77.98	26.06

subcells may also facilitate better carrier transport, contributing to the higher J_{SC}. The similarity in these efficiencies results from optimizing the bandgap of top and bottom solar cells, current matching, and minimizing optical and electrical losses, consistent with previously published work.[72,73]

Figure 5d shows the impact of top cell absorber material thickness on the standalone top PSC's PV parameters as the $CsGeI_3$ layer thickness varies from 200 to 1000 nm. As the absorber layer thickness increases, the short-circuit current density (J_{SC}) of the cell increases significantly before saturating. In contrast, the open-circuit voltage (V_{OC}) shows a slight increase from 1.060 to 1.078 V within the 100 nm−800 nm thickness range, also saturating with further increases in $CsGeI_3$ layer thickness. The thicker absorber layer enhances the photon absorption, boosting the photocurrent. However, increased thickness also leads to greater bulk recombination, which limits V_{OC}.[74] Figure 5d illustrates that the fill factor (FF) declines linearly with increasing $CsGeI_3$ layer thickness due to rising series resistance (R_S), while the power conversion efficiency (PCE) trends similarly to J_{SC}, peaking at approximately 20.8% for absorber layer thicknesses between 800 and 1000 nm.

4.2. QE Characteristic of Optimized Top and Bottom Solar Cell. Quantum efficiency is defined as the ratio of total number of electron hole pair generation to total number of photons incident into the solar cell. However, the conversion of photons into electrons at a given wavelength differs from the number of electrons successfully collected in the device electrode due to recombination losses and unabsorbed photon loss. External quantum efficiency (EQE) considers all incident light, while internal quantum efficiency (IQE) considers only absorbed photons. QE is crucial for assessing a solar cell's spectral response and overall performance.[75] QE is measured in short-circuit mode by determining the short-circuit current for monochromatic incident light. SCAPS measures the EQE because it considers the full device response to incident photons, including recombination losses but not optical reflection losses.[60]

The EQE of the solar cell is given by eq 14.

$$EQE = \frac{\Delta J_{SC}}{q\,\Delta \emptyset_{\lambda}} \tag{14}$$

Here, ΔJ_{SC} denotes the change in short-circuit current induced in a solar cell by a change in photon flux $\Delta \emptyset_{\lambda}$ at wavelength λ. Figure 6a,b shows wavelength ranges of 300−800 nm for the top PSC and 300−1200 nm for the bottom CIGS cells. It is observed that increased thickness in both cells led to higher quantum efficiency (QE). The reason is that a thicker layer enhances light absorption, especially for longer wavelengths that penetrate more deeply. This reduces the chance of photons passing through without being absorbed, thereby minimizing transmission losses. Increased photon absorption generates more electron−hole pairs, enhancing the charge carrier generation. Furthermore, a thicker absorber better utilizes the broader solar spectrum, capturing a wider range of wavelengths.[76,77] The QE of the top cell at a thickness of 1 μm varies from 97.76% to 56.88% in the wavelength range of 300−770 nm and drops to zero thereafter under the condition of negligible series resistance and very high shunt resistance. Similarly at bottom cell thickness of 2.1 μm the optimum values of QE were obtained in the range of 520 to 1100 nm under the similar condition of resistances, as shown in Figure 6 b.

4.3. Influence of the Series Resistance (R_s) and Shunt Resistance (R_{sh}) on PV Parameters and JV Characteristics. This section examines the effects of R_S and R_{Sh} on solar cell performance. Series resistance encompasses resistances from semiconductor and metal contact points along the current path, and shunt resistance is caused by leakage current across the P−N junction due to shunts at the cell periphery, crystal defects, or impurity precipitates. The two-diode model equivalent circuit of the solar cell including parasitic resistance is shown in Figure 9. R_S varies from 0.5 Ω·cm^2 to 5 Ω·cm^2, while R_{Sh} ranges from 10 Ω·cm^2 to 10^8 Ω·cm^2, allowing one to analyze the simultaneous effects of both parameters on PV performance through contour mapping, as shown in Figure 7a,b,c,d.

From Figure 7a it is observed that V_{OC} changes from 0.19 to 1.07 V, in Figure 7b J_{SC} changes from 12.86 mA/cm^2 to 19.32 mA/cm^2, in Figure 7c FF changes from 25% to 82.20%, and in Figure 7d PCE changes from 0.6% to 16.95% as R_S and R_{Sh} simultaneously change from 0.5 Ω-cm^2 to 5 Ω-cm^2 and from 10 to 10^8 Ω-cm^2, respectively. Very large R_S and very low R_{Sh} represent the straight line in the J-V curve of Figure 8a,b. Hence from Figures 7 and 8 it is concluded that a low value of

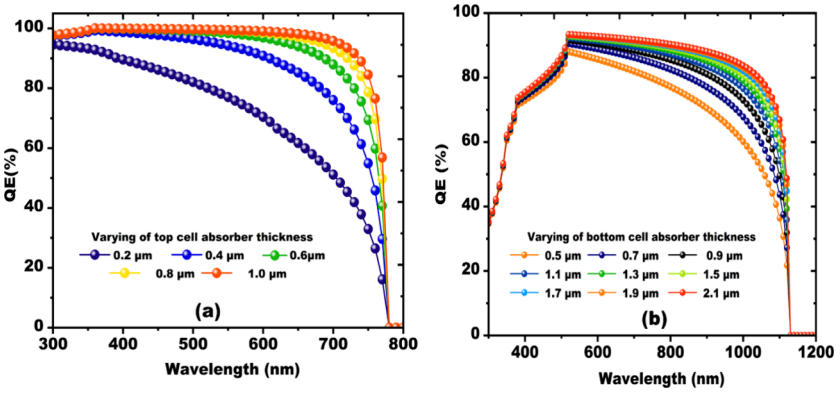

Figure 6. QE analysis by varying thickness of (a) top cell absorber and (b) bottom cell absorber

https://doi.org/10.1021/acs.langmuir.5c01551
Langmuir 2025, 41, 19729−19741

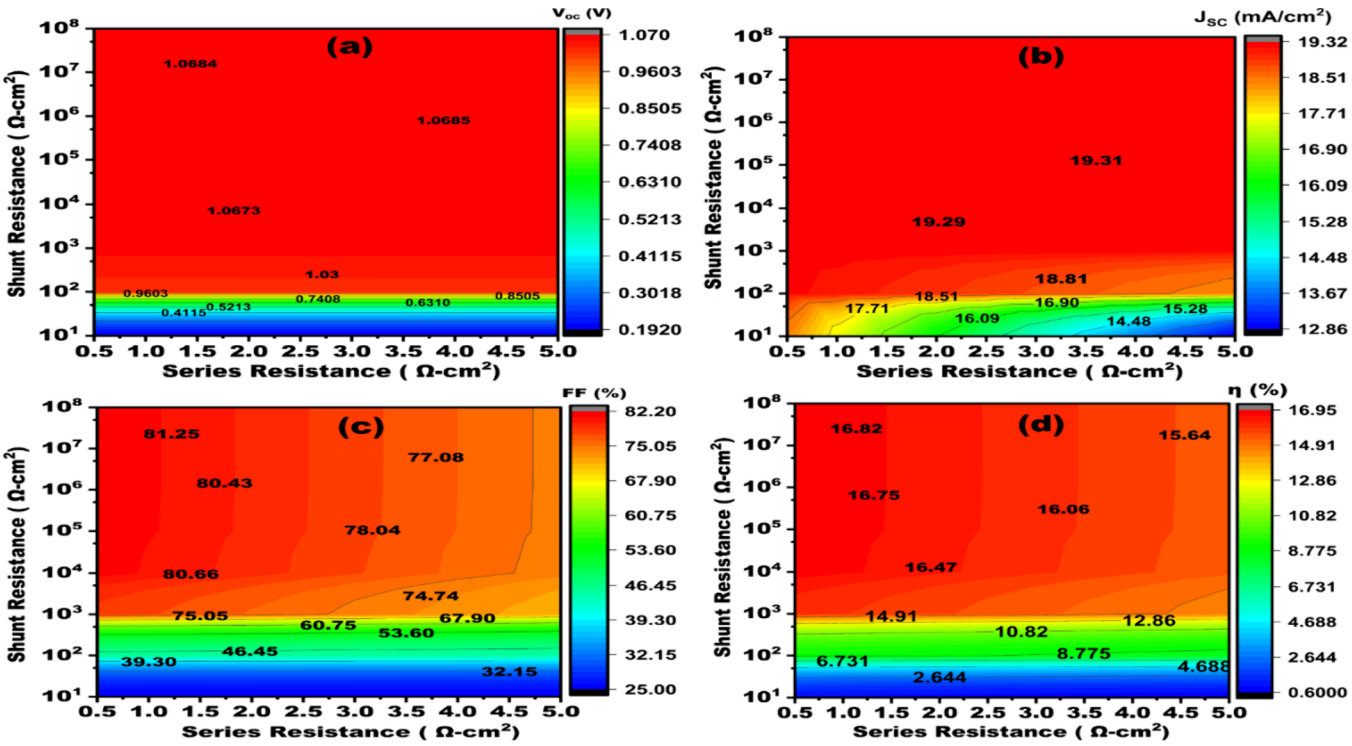

Figure 7. Parasitic resistance impact on the top cell of the PV parameters (a) V_{OC}, (b) $J_{SC,}$ (c) FF, (d) η.

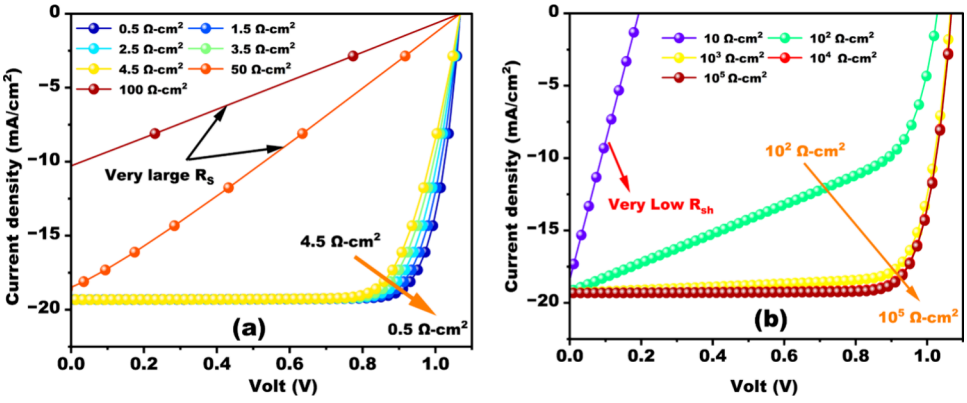

Figure 8. Effect of (a) series resistance and (b) shunt resistance on the fill factor (observe the squareness of J-V Curve) of the top solar cell.

R_S (<0.5 Ω-cm^2) and high value of R_{Sh} (>10^3 Ω-cm^2) are desirable.[78,79] Figure 8a,b illustrates how R_S and R_{Sh} affect the squareness of the J-V curve in relation to the fill factor.

The squareness of the JV curve affects the fill factors, and it is given in terms of the parasitic resistance through equations (eqs 15 and 16).[80−82]

$$FF = FF_0(1 - r_s) \tag{15}$$

$$FF = FF_0\left(1 - \frac{1}{r_{sh}}\right) \tag{16}$$

Where FF_0 represents ideal fill factor in the absence of any parasitic resistance, $r_s = R_s/R_{ch}$ and $r_{sh} = R_{sh}/R_{ch}$ are normalized series and shunt resistance, respectively, and the term R_{ch} ($R_{ch} = V_{OC}/I_{SC}$) represents the characteristic resistance of the solar cells.

The two-diode model of the solar cell circuit diagram accurately represents electrical behavior by accounting for nonideal effects such as recombination losses and leakage currents. This model is crucial for optimizing solar cell design and enhancing efficiency, offering a thorough understanding of the performance under real-world conditions. In Figure 9, J_{01} and J_{02} represent the saturation current densities as a recombination in base emitter and space charge region, I is the current across R_S, and V is the output voltage.

4.4. Impact of Temperature and Absorption Coefficients of Top Cell. Figure 10a depicts the J-V curve performance of tandem solar cell for different temperatures. Solar cell performance declines with rising temperature primarily due to increased internal carrier recombination driven by higher carrier concentrations. This reduces the built-in potential across the $P-N$ junction, which lowers the open-circuit voltage (V_{OC}). Operating temperature is therefore critical for photovoltaic conversion.[83−87] The temperature dependence of the solar cell performance comes from the dependency of V_{OC} on temperature that depends on the reverse saturation current (I_0) according to eq 17.

https://doi.org/10.1021/acs.langmuir.5c01551
Langmuir 2025, 41, 19729−19741

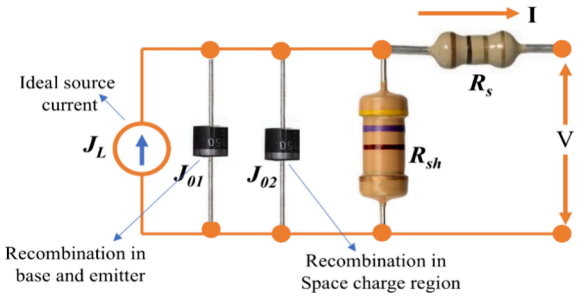

Figure 9. Two-diode model equivalent circuit of the solar cell.

$$I_0 \propto e^{-E_g/kT} \tag{17}$$

In Figure 10a, device performance is analyzed by varying the operating temperature from 300 to 400 K. The plot indicates that V_{OC} decreases as temperature increases, likely due to the rise in intrinsic carrier concentration (n_i) and resulting increase in reverse saturation current. Intrinsic carrier density is dependent on the semiconductor material's bandgap energy (E_g) and temperature (T) given by eq 18, and the expression for V_{OC} is given by eq 19.[88]

$$n_i^2 \propto e^{-E_g/kT} \tag{18}$$

$$V_{OC} = \frac{kT}{q} \times \ln \frac{I_{SC}/I_0}{q} \tag{19}$$

In Figure 10a the area under the JV curve decreases as temperature increases, which reduces the open-circuit voltage and hence the overall performance of the SC affected. Figure 10b indicates that the absorption coefficients of each layer of the top solar cell were calculated from eq 12 and later these coefficients are used for calculation of the filtered spectrum to study the bottom cell performance. The absorption coefficient quantifies how deeply light of a given wavelength penetrates a material before being absorbed. Different wavelengths penetrate at different depths, impacting the generation of electron–hole pairs. The graph demonstrates that even above the band gap, the absorption coefficient varies significantly with wavelength. Photon absorption depends on the probability of a photon interacting with an electron to facilitate a transition between energy bands. Near the band gap energy, absorption is lower because only electrons at the valence band edge can participate. As photon energy increases beyond this, more electrons become capable of interaction, leading to higher absorption.[89,90]

5. COMPARISON TO SIMILAR WORKS

This work focuses on the optimization of an environmentally friendly $CsGeI_3$/CIGS tandem solar cell, aiming to establish it as a potential alternative to its lead-based counterparts. The performance potential is evaluated using four key parameters: J_{SC}, V_{OC}, FF, and PCE, benchmarked against recently reported values in the literature. For comparison, in the earliest published work the highest reported J_{SC}, V_{OC}, FF, and PCE for a Pb-based perovskite/CIGS tandem solar cell are 19.24 mA/cm^2, 1.768 V, 72.9%, and 24.2%.[91] In this work, the $CsGeI_3$/CIGS tandem achieved J_{SC}, V_{OC}, FF, and PCE values of 19.32 mA/cm^2, 1.73 V, 77.98%, and 26.06%, respectively. Additionally, when compared to the Shockley–Queisser (SQ) limit (~33%) for a single-junction solar cell with a 1.1 eV bandgap (CIGS), the proposed tandem device shows nearly 0.41%, 6.51%, and 7.13% improvement in J_{SC}, FF, and PCE, respectively, while V_{OC} reduces to 2.14%. The one possible reason could be for decrease in V_{OC} is higher nonradiative recombination particularly at interfaces and defects, lowering V_{OC} by reducing charge carrier lifetime. High series resistance in contacts or layers can limit charge extraction, negatively impacting V_{OC}. A comprehensive comparison of this work to similar reports in the literature is shown in Table 4.

Table 4. Comparison of Current Work with Earlier Published Work

Top/Bottom subcells	V_{OC} (V)	J_{SC} (mA/cm^2)	FF (%)	PCE (%)	ref
CIGS/$CsGeI_3$	1.73	19.32	77.98	26.06	This work
Cs(MAFA)Pb(IBr)/ CIGS	1.04	19.24	72.9	24.2	91
CIGS/ $Cu_2ZnSn(S,Se)_4$	1.45	16.1	68.2	15.90	92
$CsGeI_3$/c-Si	1.90	17.55	84.9	28.43	35
CIGS/SWCNT	1.34	37.87	76.41	38.91	66
CIGS/Si	1.45	16.70	81.50	19.80	93
$CsGeI_3$/$FASnI_3$	2.12	16.71	85.87	30.42	38
$CsGeI_3$/ $CsGeI_2Br$	1.22	32.79	79.19	31.86	42
$CsGeI_3$/$CsPbI_3$	1.04	20.70	67.72	14.63	94

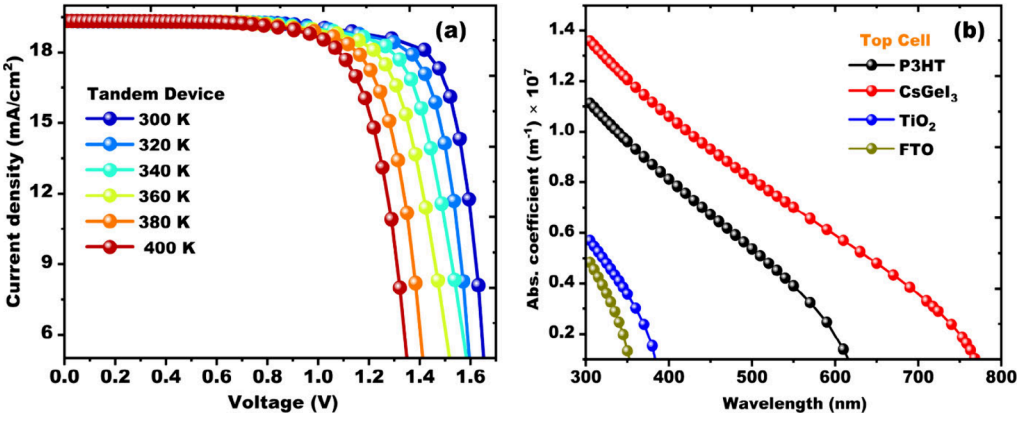

Figure 10. (a) Impact of temperature on J-V characteristics of tandem solar cell. (b) The absorption coefficient analysis for top solar cell layers including P3HT, $CsGeI_3$, TiO_2, and FTO used during simulation and for calculation of filtered spectrum (Taken from SCAPS database file).

https://doi.org/10.1021/acs.langmuir.5c01551
Langmuir 2025, 41, 19729–19741

The performance parameters of the CIGS/$CsGeI_3$ solar cell reported in this work showcase a significant position among the tandem solar cells reported in the literature.

6. CONCLUSIONS

This work concludes the photovoltaic performance of a two-terminal $CsGeI_3$/CIGS tandem solar cell (TSC) that demonstrates a power conversion efficiency (PCE) of 26.06% (J_{SC} = 19.32 mA/cm^2, V_{OC} = 1.73 V, FF = 77.98%), establishing it as a promising lead-free alternative for high-efficiency photovoltaics. Optimized standalone top and bottom cell thicknesses of 273 and 1000 nm absorber layers achieved PCEs of 16.93% and 16.49%, respectively. The simulations were calibrated with experimental data for both cells to ensure the accuracy of the simulation and were also compared with the experimental findings. This study investigates the impact of various parameters, including layer thickness, parasitic resistance, temperature, quantum efficiency, band diagram, absorption coefficients, and two-diode model equivalent circuit, on the solar cell performance. This tandem design presents a pathway for developing efficient and cost-effective perovskite-CIGS tandem solar cells, with the reported performance representing a record for this device structure and a potential alternative to lead-free tandem solar cells. Future work may explore the impact of the tunnel recombination junction. We also believe that our approach will advance high-performance PSC/CIGS tandem solar cell development and broaden their application in building-integrated photovoltaics.

■ ASSOCIATED CONTENT

Data Availability Statement

Data will be made available on request.

■ AUTHOR INFORMATION

Corresponding Author

Sushama M. Giripunje − *Nanomaterials and Energy Harvesting Devices Laboratory, Department of Physics, Visvesvaraya National Institute of Technology, Nagpur, Maharashtra 440010, India;* orcid.org/0009-0004-7265-0018; Phone: 0712-2801171; Email: profsmgphysics2047@gmail.com

Authors

Alok Kumar − *Nanomaterials and Energy Harvesting Devices Laboratory, Department of Physics, Visvesvaraya National Institute of Technology, Nagpur, Maharashtra 440010, India*

Mukesh Bharadwaj − *National Institute of Technology Raipur, Raipur, Chhattisgarh 492010, India*

Deboraj Muchahary − *National Institute of Technology Raipur, Raipur, Chhattisgarh 492010, India*

Complete contact information is available at: https://pubs.acs.org/10.1021/acs.langmuir.5c01551

Notes

The authors declare no competing financial interest.

■ ACKNOWLEDGMENTS

The authors express their sincere gratitude to Professor Marc Burgelman and his team at the Department of Electronics and Information Systems, University of Ghent, Belgium for developing this amazing simulation tool and Centre of Nanotechnology at IIT Guwahati for providing the training program on simulation software under the Indian nano-electronics user program (INUP) which is run by the Ministry of Electronics and Information Technology (MeitY), Government of the Republic of India.

■ REFERENCES

(1) Monnaf, M. A.; Ghosh, A.; Nabil, S. H.; Islam, M. B.; Rashid, T.; Al Fathah, A.; Alam, K.; Alturaifi, H. A.; Awwad, N. S. The Development and Evaluation of Hybrid Solar Cells Based on Perovskites and CIGS with Different ETL for Increased Photovoltaic Efficiency Using SCAPS-1D. *Langmuir* **2025**, *41*, 12556.

(2) Jošt, M.; Köhnen, E.; Al-Ashouri, A.; Bertram, T.; Tomšič, Š.; Magomedov, A.; Kasparavicius, E.; Kodalle, T.; Lipovšek, B.; Getautis, V.; Schlatmann, R.; Kaufmann, C. A.; Albrecht, S.; Topič, M. Perovskite/CIGS Tandem Solar Cells: From Certified 24.2% toward 30% and Beyond. *ACS Energy Letters* **2022**, *7* (4), 1298−1307.

(3) Chipangamate, N. S.; Nwaila, G. T. Assessment of Challenges and Strategies for Driving Energy Transitions in Emerging Markets: A Socio-Technological Systems Perspective. *Energy Geoscience* **2024**, *5* (2), No. 100257.

(4) Olaleru, S. A.; Kirui, J. K.; Wamwangi, D.; Roro, K. T.; Mwakikunga, B. Perovskite Solar Cells: The New Epoch in Photovoltaics. *Sol. Energy* **2020**, *196*, 295−309.

(5) Hammarström, L. Overview: Capturing the Sun for Energy Production. *AMBIO* **2012**, *41* (2), 103−107.

(6) Aramendia, E.; Brockway, P. E.; Taylor, P. G.; Norman, J. B.; Heun, M. K.; Marshall, Z. Estimation of Useful-Stage Energy Returns on Investment for Fossil Fuels and Implications for Renewable Energy Systems. *Nature Energy* **2024**, *9*, 803−816.

(7) Battaglia, C.; Cuevas, A.; De Wolf, S. High-Efficiency Crystalline Silicon Solar Cells: Status and Perspectives. *Energy Environ. Sci.* **2016**, *9* (5), 1552−1576.

(8) Chowdhury, S.; Kumar, M.; Dutta, S.; Park, J.; Kim, J.; Kim, S.; Ju, M.; Kim, Y.; Cho, Y.; Cho, E.-C.; Yi, J. High-Efficiency Crystalline Silicon Solar Cells: A Review. *New & Renewable Energy* **2019**, *15* (3), 36−45.

(9) Global news. At 26.81%, LONGi Sets a New World Record Efficiency for Silicon Solar Cells. *Longi* **2022**, 1−5.

(10) Shockley, W.; Queisser, H. J. Detailed Balance Limit of Efficiency of P-n Junction Solar Cells. *J. Appl. Phys.* **1961**, *32* (3), 510−519.

(11) Heidarzadeh, H.; Rostami, A.; Dolatyari, M. Management of Losses (Thermalization-Transmission) in the Si-QDs inside 3C−SiC to Design an Ultra-High-Efficiency Solar Cell. *Materials Science in Semiconductor Processing* **2020**, *109*, No. 104936. (May 2019)

(12) Jackson, E. D. Areas for Improvement of the Semiconductor Solar Energy Converter. *Trans. Int. Conf. on the Use of Solar Energy-The Scientific Basis* **1955**, *5*, 122.

(13) Wang, R.; Huang, T.; Xue, J.; Tong, J.; Zhu, K.; Yang, Y. Prospects for Metal Halide Perovskite-Based Tandem Solar Cells. *Nat. Photonics* **2021**, *15* (6), 411−425.

(14) Lamorte, M. F.; Abbott, D. H. Computer Modeling of a Two-Junction, Monolithic Cascade Solar Cell. *IEEE Trans. Electron Devices* **1980**, *27* (1), 231−249.

(15) Kim, K.; Gwak, J.; Ahn, S. K.; Eo, Y. J.; Park, J. H.; Cho, J. S.; Kang, M. G.; Song, H. E.; Yun, J. H. Simulations of Chalcopyrite/c-Si Tandem Cells Using SCAPS-1D. *Sol. Energy* **2017**, *145*, 52−58.

(16) Mousa, M.; Amer, F. Z.; Mubarak, R. I.; Saeed, A. Simulation of Optimized High-Current Tandem Solar-Cells with Efficiency beyond 41%. *IEEE Access* **2021**, *9*, 49724−49737.

(17) Yamaguchi, M.; Dimroth, F.; Geisz, J. F.; Ekins-Daukes, N. J. Multi-Junction Solar Cells Paving the Way for Super High-Efficiency. *J. Appl. Phys.* **2021**, *129* (24), 1−15.

(18) Shi, Y.; Berry, J. J.; Zhang, F. Perovskite/Silicon Tandem Solar Cells: Insights and Outlooks. *ACS Energy Letters* **2024**, *9* (3), 1305−1330.

(19) Harter, A.; Artuk, K.; Mathies, F.; Karalis, O.; Hempel, H.; Al-Ashouri, A.; Albrecht, S.; Schlatmann, R.; Ballif, C.; Stannowski, B.; Wolff, C. M. Perovskite/Silicon Tandem Solar Cells Above 30% Conversion Efficiency on Submicron-Sized Textured Czochralski-Silicon Bottom Cells with Improved Hole-Transport Layers. *ACS Appl. Mater. Interfaces* **2024**, *16* (45), 62817−62826.
(20) Mohamad Noh, M. F.; Arzaee, N. A.; Fat, C. C.; Sieh Kiong, T.; Mat Teridi, M. A.; Mahmood Zuhdi, A. W. Perovskite/CIGS Tandem Solar Cells: Progressive Advances from Technical Perspectives. *Materials Today Energy* **2024**, *39*, 101473.
(21) Madan, J.; Shivani; Pandey, R.; Sharma, R. Device Simulation of 17.3% Efficient Lead-Free All-Perovskite Tandem Solar Cell. *Sol. Energy* **2020**, *197* (197), 212−221.
(22) Eperon, G. E.; Leijtens, T.; Bush, K. A.; Prasanna, R.; Green, T.; Wang, J. T.-W.; McMeekin, D. P.; Volonakis, G.; Milot, R. L.; May, R.; Palmstrom, A.; Slotcavage, D. J.; Belisle, R. A.; Patel, J. B.; Parrott, E. S.; Sutton, R. J.; Ma, W.; Moghadam, F.; Conings, B.; Babayigit, A.; Boyen, H.-G.; Bent, S.; Giustino, F.; Herz, L. M.; Johnston, M. B.; McGehee, M. D.; Snaith, H. J. Perovskite-Perovskite Tandem Photovoltaics with Optimized Band Gaps. *Science* **2016**, *354* (6314), 861−865.
(23) Forgács, D.; Gil-Escrig, L.; Pérez-Del-Rey, D.; Momblona, C.; Werner, J.; Niesen, B.; Ballif, C.; Sessolo, M.; Bolink, H. J. Efficient Monolithic Perovskite/Perovskite Tandem Solar Cells. *Adv. Energy Mater.* **2017**, *7* (8), 1−6.
(24) Hossain, M. I.; Saleque, A. M.; Ahmed, S.; Saidjafarzoda, I.; Shahiduzzaman, M.; Qarony, W.; Knipp, D.; Biyikli, N.; Tsang, Y. H. Perovskite/Perovskite Planar Tandem Solar Cells: A Comprehensive Guideline for Reaching Energy Conversion Efficiency beyond 30%. *Nano Energy* **2021**, *79*, No. 105400. (August 2020)
(25) Mailoa, J. P.; Bailie, C. D.; Johlin, E. C.; Hoke, E. T.; Akey, A. J.; Nguyen, W. H.; McGehee, M. D.; Buonassisi, T. A 2-Terminal Perovskite/Silicon Multijunction Solar Cell Enabled by a Silicon Tunnel Junction. *Appl. Phys. Lett.* **2015**, *106* (12). DOI: 10.1063/1.4914179.
(26) Shivarudraiah, S. B.; Ng, M.; Li, C. H. A.; Halpert, J. E. All-Inorganic, Solution-Processed, Inverted CsPbI3Quantum Dot Solar Cells with a PCE of 13.1% Achieved via a Layer-by-Layer FAI Treatment. *ACS Applied Energy Materials* **2020**, *3* (6), 5620−5627.
(27) Hu, L.; Wang, Y.; Shivarudraiah, S. B.; Yuan, J.; Guan, X.; Geng, X.; Younis, A.; Hu, Y.; Huang, S.; Wu, T.; Halpert, J. E. Quantum-Dot Tandem Solar Cells Based on a Solution-Processed Nanoparticle Intermediate Layer. *ACS Appl. Mater. Interfaces* **2020**, *12* (2), 2313−2318.
(28) Azhakanantham, D.; Selvamani, M.; Geun Kim, T.; Contreras, D.; Varman Kesavan, A. Exploring Novel HTL Suitable for Eco-Friendly and High Performance FASnI3 Photovoltaics. *Materials Science and Engineering: B* **2022**, *284* (July), No. 115909.
(29) Hu, S.; Li, W.; Liu, S.; Zhou, Z.; Zhang, Y.; Luo, Z.; Jin, H.; Jin, Q.; Hou, Y.; Zhou, X.; Wang, Z. *Flexible Perovskite-Based Multiple-Junction Photovoltaics. Joule* **2025**, *9* (3), No. 101870.
(30) Tong, J.; Song, Z.; Kim, D. H.; Chen, X.; Chen, C.; Palmstrom, A. F.; Ndione, P. F.; Reese, M. O.; Dunfield, S. P.; Reid, O. G.; Liu, J.; Zhang, F.; Harvey, S. P.; Li, Z.; Christensen, S. T.; Teeter, G.; Zhao, D.; Al-Jassim, M. M.; Van Hest, M. F. A. M.; Beard, M. C.; Shaheen, S. E.; Berry, J. J.; Yan, Y.; Zhu, K. Carrier Lifetimes of > 1 Ms in Sn-Pb Perovskites Enable Efficient All-Perovskite Tandem Solar Cells. *Science* **2019**, *364* (6439), 475−479.
(31) Xiong, Y.; Yi, Z.; Zhang, W.; Huang, Y.; Zhang, Z.; Jiang, Q.; Ng, X. R.; Shen, G.; Luo, Y.; Li, X.; Yang, J. Recent Advances in Perovskite/Cu(In,Ga)Se2 Tandem Solar Cells. *Materials Today Electronics* **2024**, *7*, 100086.
(32) Gezgin, S. Y.; Houimi, A.; Gündoğdu, Y.; Mercimek, B.; Kılıç, H. Ş. Determination of Photovoltaic Parameters of CIGS Hetero Junction Solar Cells Produced by PLD Technique, Using SCAPS Simulation Program. *Vacuum* **2021**, *192* (July), 110451.
(33) Liu, W.; Li, H.; Qiao, B.; Zhao, S.; Xu, Z.; Song, D. Highly Efficient CIGS Solar Cells Based on a New CIGS Bandgap Gradient Design Characterized by Numerical Simulation. *Sol. Energy* **2022**, *233* (233), 337−344. (September 2021),
(34) Lu, J.; Chen, S.; Wang, H.; Qiu, L.; Wu, C.; Qian, W.; Wang, Z.; Huang, K.; Wu, J.; Chen, H.; Gao, Y. Replacing the Electron-Hole Transport Layer with Doping: SCAPS Simulation of Lead-Free Germanium-Based Perovskite Solar Cells Based on CsGeI3. *Sol. Energy Mater. Sol. Cells* **2024**, *271* (April), No. 112883.
(35) Ravidas, B. K.; Das, A.; Agnihotri, S. K.; Pandey, R.; Madan, J.; Hossain, M. K.; Roy, M. K.; Samajdar, D. P. Design Principles of Crystalline Silicon/CsGeI3 Perovskite Tandem Solar Cells Using a Combination of Density Functional Theory and SCAPS-1D Frameworks. *Sol. Energy Mater. Sol. Cells* **2024**, *267*, No. 112688.
(36) MallaHasan, H.; Onay, Ö. Investigation of the Effect of Different Factors on the Performance of Several Perovskite Solar Cells: A Simulation Study by SCAPS. *European Journal of Engineering Science and Technology* **2023**, *5* (1), 20−38.
(37) Vanitha, L.; Sahoo, S.; Prabu, R. T.; Kumar, A. Performance Analysis of Wide Bandgap Inorganic Perovskite for Indoor Photovoltaics for IoT Applications: Simulation Study. *Optical and Quantum Electronics* **2024**, *56* (9), 1−15.
(38) El Arfaoui, Y.; Khenfouch, M.; Habiballah, N. Optimization of All Pb-Free Perovskite CsGeI3/FASnI3 Tandem Solar Device with 30.42% Efficiency: Numerical Simulation Using SCAPS. *Optik* **2024**, *300* (300), No. 171638.
(39) Song, J.; Qiu, L.; Ding, C.; Jin, S.; Wang, J.; Huang, K.; Huang, H.; Wu, J.; Zhang, R.; Sheng, K.; Yang, X. Numerical Simulation and Performance Optimization of All-Inorganic CsGeI3 Perovskite Solar Cells with Stacked ETLs/C60 by SCAPS Device Simulation. *Materials Today Communications* **2024**, *38* (2103), No. 108587.
(40) Tara, A.; Bharti, V.; Sharma, S.; Gupta, R. Computational Approach to Explore Suitable Charge Transport Layers for All Inorganic CsGeI3 Perovskite Solar Cells. *Opt. Mater.* **2022**, *128*, No. 112403.
(41) Zhang, Y.; Meng, X.; Liu, X.; Zhou, F.; Yang, W.; Fan, Y.; He, P.; Wu, J.; Wang, H.; Cheng, Y. SCAPS Simulation and DFT Study of Lead-Free Perovskite Solar Cells Based on CsGeI3. *Mater. Chem. Phys.* **2023**, *306* (May), No. 128084.
(42) Kenfack, A. D. K.; Thantsha, N. M.; Msimanga, M. Simulation of Lead-Free Heterojunction CsGeI2Br/CsGeI3-Based Perovskite Solar Cell Using SCAPS-1D. *Solar* **2023**, *3* (3), 458−472.
(43) Raj, A.; Kumar, M.; Bherwani, H.; Gupta, A.; Anshul, A. Evidence of Improved Power Conversion Efficiency in Lead-Free CsGeI3 Based Perovskite Solar Cell Heterostructure via Scaps Simulation. *Journal of Vacuum Science & Technology B, Nanotechnology and Microelectronics: Materials, Processing, Measurement, and Phenomena* **2021**, *39* (1). DOI: 10.1116/6.0000718.
(44) Keller, J.; Kiselman, K.; Donzel-Gargand, O.; Martin, N. M.; Babucci, M.; Lundberg, O.; Wallin, E.; Stolt, L.; Edoff, M. High-Concentration Silver Alloying and Steep Back-Contact Gallium Grading Enabling Copper Indium Gallium Selenide Solar Cell with 23.6% Efficiency. *Nature Energy* **2024**, *9* (April), 467.
(45) Ramanujam, J.; Bishop, D. M.; Todorov, T. K.; Gunawan, O.; Rath, J.; Nekovei, R.; Artegiani, E.; Romeo, A. Flexible CIGS, CdTe and a-Si:H Based Thin Film Solar Cells: A Review. *Prog. Mater. Sci.* **2020**, *110*, No. 100619.
(46) Salhi, B. The Photovoltaic Cell Based on CIGS: Principles and Technologies. *Materials* **2022**, *15* (5), 1908.
(47) Mwenda, P. M.; Njoroge, W.; Mirenga, S.; Kinyua, D. M. Review: Advances in the CIGS Thin Films for Photovoltaic Applications. *Smart Grid and Renewable Energy* **2022**, *13* (04), 75−87.
(48) Su, P.; Liu, Y.; Zhang, J.; Chen, C.; Yang, B.; Zhang, C.; Zhao, X. Pb-Based Perovskite Solar Cells and the Underlying Pollution behind Clean Energy: Dynamic Leaching of Toxic Substances from Discarded Perovskite Solar Cells. *J. Phys. Chem. Lett.* **2020**, *11* (8), 2812−2817.
(49) Ali, R.; Hou, G.-J.; Zhu, Z.-G.; Yan, Q.-B.; Zheng, Q.-R.; Su, G. Stable Mixed Group II (Ca, Sr) and XIV (Ge, Sn) Lead-Free Perovskite Solar Cells. *Journal of Materials Chemistry A* **2018**, *6* (19), 9220−9227.

(50) Pan, Y.; Zhu, M.; Lv, Y.; Yang, Y.; Liang, Y.; Yin, R.; Yang, Y.; Jia, X.; Wang, X.; Zeng, F.; Huang, S.; Hou, D.; Xu, L.; Yin, R.; Yuan, X. Building Energy Simulation and Its Application for Building Performance Optimization: A Review of Methods, Tools, and Case Studies. *Advances in Applied Energy* **2023**, *10*, No. 100135.
(51) Karthick, S.; Velumani, S.; Bouclé, J. Experimental and SCAPS Simulated Formamidinium Perovskite Solar Cells: A Comparison of Device Performance. *Sol. Energy* **2020**, *205* (May), 349−357.
(52) Yadav, R. K.; Pawar, P. S.; Nandi, R.; Neerugatti, K. R. E.; Kim, Y. T.; Cho, J. Y.; Heo, J. A Qualitative Study of SnSe Thin Film Solar Cells Using SCAPS 1D and Comparison with Experimental Results: A Pathway towards 22.69% Efficiency. *Sol. Energy Mater. Sol. Cells* **2022**, *244*, No. 111835. (June),
(53) Seyed-Talebi, S. M.; Lee, C. H. Nitrogen-Doped Titanium Dioxide as a Novel Eco-Friendly Hole Transport Layer in Lead-Free CsSnI3 Based Perovskite Solar Cells. *Mater. Res. Bull.* **2024**, *172*, No. 112642. (December 2023)
(54) Ahmmed, S.; Aktar, A.; Tabassum, S.; Rahman, M. H.; Rahman, M. F.; Md Ismail, A. B. CuO Based Solar Cell with V2O5 BSF Layer: Theoretical Validation of Experimental Data. *Superlattices Microstruct.* **2021**, *151*, No. 106830.
(55) Nelson, J. *The Physics Of Solar Cells* **2003**, 79−117.
(56) Priyanka, E.; Muchahary, D. Performance Improvement of Perovskite/CIGS Tandem Solar Cell Using Barium Stannate Charge Transport Layer and Achieving PCE of 39% Numerically. *Sol. Energy* **2024**, *267*, No. 112218. (November 2023)
(57) Patel, A. K.; Mishra, R.; Soni, S. K.; Rao, P. K.; Mishra, O. Design and Performance Investigation of CIGS/SWCNT Tandem Solar Cell for Efficiency Improvement. *Opt. Commun.* **2024**, *559* (Feb), No. 130392.
(58) Singh, Y. K.; Dwivedi, D. K.; Lohia, P.; Pandey, R.; Madan, J.; Agarwal, S.; Yadav, R. K.; Alsaif, F.; Hossain, M. K. Current Matching and Filtered Spectrum Analysis of Wide-Bandgap/Narrow-Bandgap Perovskite/CIGS Tandem Solar Cells: A Numerical Study of 34.52% Efficiency Potential. *J. Phys. Chem. Solids* **2025**, *196*, No. 112300.
(59) Kumar, A.; Giripunje, S. M.; Patel, A. K.; Gohri, S. Simulation Study of Cadmium-Free CIGS Solar Cell for Efficiency Enhancement by Minimizing Recombination Losses through Back Surface Field Mechanism. *Solid State Commun.* **2024**, *394*, No. 115694.
(60) Burgelman, M.; Decock, K.; Niemegeers, A.; Verschraegen, J.; Degrave, S. *Scaps Manual.* **2024**, 4−10.
(61) Chen, L. J. Synthesis and Optical Properties of Lead-Free Cesium Germanium Halide Perovskite Quantum Rods. *RSC Adv.* **2018**, *8* (33), 18396−18399.
(62) HOSSEİNİ, S.; DELİBAŞ, N.; BAHRAMGOUR, M.; TABATABAEİ MASHAYEKH, A.; NİAİE, A. Performance Comparison of Different Hole Transport Layer Configurations in a Perovskite-Based Solar Cell Using SCAPS-1D Simulation. *European Journal of Science and Technology* **2021**, *31* (31), 121−126.
(63) Li, S.; Cao, Y. L.; Li, W. H.; Bo, Z. S. A Brief Review of Hole Transporting Materials Commonly Used in Perovskite Solar Cells. *Rare Metals* **2021**, *40* (10), 2712−2729.
(64) Kato, T.; Wu, J. L.; Hirai, Y.; Sugimoto, H.; Bermudez, V. Record Efficiency for Thin-Film Polycrystalline Solar Cells Up to 22.9% Achieved by Cs-Treated Cu(In,Ga)(Se,S)2. *IEEE Journal of Photovoltaics* **2019**, *9* (1), 325−330.
(65) Priyanka, E.; Muchahary, D. Performance Improvement of Perovskite/CIGS Tandem Solar Cell Using Barium Stannate Charge Transport Layer and Achieving PCE of 39% Numerically. *Sol. Energy* **2024**, *267*, No. 112218. (June 2023)
(66) Patel, A. K.; Mishra, R.; Soni, S. K.; Rao, P. K.; Mishra, O. Design and Performance Investigation of CIGS/SWCNT Tandem Solar Cell for Efficiency Improvement. *Opt. Commun.* **2024**, *559*, No. 130392. (December 2023)
(67) Shrivastav, N.; Kashyap, S.; Madan, J.; Al-Mousoi, A. K.; Mohammed, M. K. A.; Hossain, M. K.; Pandey, R.; Ramanujam, J. Perovskite-CIGS Monolithic Tandem Solar Cells with 29.7% Efficiency: A Numerical Study. *Energy Fuels* **2023**, *37* (4), 3083−3090.
(68) Eom, K.; Kwon, U.; Kalanur, S. S.; Park, H. J.; Seo, H. Depth-Resolved Band Alignments of Perovskite Solar Cells with Significant Interfacial Effects. *Journal of Materials Chemistry A* **2017**, *5* (6), 2563−2571.
(69) Wurfel, U.; Cuevas, A.; Wurfel, P. Charge Carrier Separation in Solar Cells. *IEEE Journal of Photovoltaics* **2015**, *5* (1), 461−469.
(70) Islam, M. T.; Jani, M. R.; Islam, A. F.; Shorowordi, K. M.; Chowdhury, S.; Nishat, S. S.; Ahmed, S. Investigation of CsSn0.5Ge0.5I3-on-Si Tandem Solar Device Utilizing SCAPS Simulation. *IEEE Trans. Electron Devices* **2021**, *68* (2), 618−625.
(71) Kumar, A.; Giripunje, S. M.; Patel, A. K.; Gohri, S. Designing and Simulating of New Highly Efficient Ultra-Thin CIGS Solar Cell Device Structure: Plan to Minimize Cost per Watt Price. *J. Phys. Chem. Solids* **2024**, *193* (June), No. 112194.
(72) Kumar, P.; Kumar, A. Double Perovskite Tandem Solar Cells: Design and Performance Investigation of the Use of CABB and CCSC as Top and Bottom Cell Absorber Materials. *J. Electron. Mater.* **2024**, *53* (6), 2736−2752.
(73) Liu, X.; Zhang, J.; Tang, L.; Gong, J.; Li, W.; Ma, Z.; Tu, Z.; Li, Y.; Li, R.; Hu, X.; Shen, C.; Wang, H.; Wang, Z.; Lin, Q.; Fang, G.; Wang, S.; Liu, C.; Zhang, Z.; Li, J.; Xiao, X. Over 28% Efficiency Perovskite/Cu(InGa)Se2 Tandem Solar Cells: Highly Efficient Sub-Cells and Their Bandgap Matching. *Energy Environ. Sci.* **2023**, *16* (11), 5029−5042.
(74) Jiang, M.; Tang, J. Simulated Development and Optimized Performance of Narrow-Bandgap CsSnI3-Based All-Inorganic Perovskite Solar Cells. *J. Phys. D: Appl. Phys.* **2021**, *54* (46), No. 465104.
(75) Farah Khaleda, M. Z.; Vengadaesvaran, B.; Rahim, N. A. *Chapter 18 - Spectral Response and Quantum Efficiency Evaluation of Solar Cells: A Review*; Dhoble, S. J., Kalyani, N. T., Vengadaesvaran, B., Kariem Arof, A. B. T.-E. M., Eds.; Elsevier, 2021; pp 525−566. DOI: 10.1016/B978-0-12-823710-6.00014-5.
(76) Yang, W. J.; Ma, Z. Q.; Tang, X.; Feng, C. B.; Zhao, W. G.; Shi, P. P. Internal Quantum Efficiency for Solar Cells. *Sol. Energy* **2008**, *82* (2), 106−110.
(77) Karmalawi, A. M.; Rayan, D. A.; Rashad, M. M. Establishment and Evaluation of Photovoltaic Quantum Efficiency System at Central Metallurgical Research and Development Institute. *Optik* **2020**, *217*, No. 164931.
(78) Sardar, R. H.; Bera, A.; Chattopadhyay, S.; Ali, S. I.; Pramanik, S.; Mandal, A. C. The Impact of Series (Rs) and Shunt Resistances (Rsh) on Solar Cell Parameters to Enhance the Photovoltaic Performance of f-PSCs. *Opt. Mater.* **2024**, *155*, No. 115818.
(79) Singh, P.; Ravindra, N. M. Analysis of Series and Shunt Resistance in Silicon Solar Cells Using Single. *Emerging Materials Research* **2012**, *1*, 33−38.
(80) Ghani, F.; Duke, M.; Carson, J. Numerical Calculation of Series and Shunt Resistances and Diode Quality Factor of a Photovoltaic Cell Using the Lambert W-Function. *Sol. Energy* **2013**, *91*, 422−431.
(81) Green, M. A. Accurate Expressions for Solar Cell Fill Factors Including Series and Shunt Resistances. *Appl. Phys. Lett.* **2016**, *108* (8), 81111.
(82) Tada, K. What Do Apparent Series and Shunt Resistances in Solar Cell Estimated by I−V Slope Mean? Study with Exact Analytical Expressions. *Physica Status Solidi (A) Applications and Materials Science* **2018**, *215* (23), 1−4.
(83) Fathi, M.; Abderrezek, M.; Djahli, F.; Ayad, M. Study of Thin Film Solar Cells in High Temperature Condition. *Energy Procedia* **2015**, *74*, 1410−1417.
(84) Abderrezek, M.; Fathi, M.; Djahli, F. Comparative Study of Temperature Effect on Thin Film Solar Cells. *Journal of Nano- and Electronic Physics* **2018**, *10* (2), 1−6.
(85) Lin, L.; Ravindra, N. M. Temperature Dependence of CIGS and Perovskite Solar Cell Performance: An Overview. *SN Applied Sciences* **2020**, *2* (8), 1−12.
(86) Ravindra, N. M.; Srivastava, V. K. Temperature Dependence of the Energy Gap in Semiconductors. *J. Phys. Chem. Solids* **1979**, *40* (10), 791−793.

(87) Al-naser, Q. A. H.; Al-barghoothi, N. M. A.; Al-ali, N. A. S. The Effect of Temperature Variations on Solar Cell Efficiency. *International Journal of Engineering, Business and Enterprise Applications (IJEBEA)* **2013**, 108−112 No. July 2012,.
(88) Radziemska, E. Thermal Performance of Si and GaAs Based Solar Cells and Modules: A Review. *Prog. Energy Combust. Sci.* **2003**, *29* (5), 407−424.
(89) Kumar, D.; Bansal, N. K.; Dixit, H.; Kulkarni, A.; Singh, T. Numerical Study on the Effect of Dual Electron Transport Layer in Improving the Performance of Perovskite−Perovskite Tandem Solar Cells. *Advanced Theory and Simulations* **2023**, *6* (3). DOI: 10.1002/adts.202200800.
(90) Chen, E. M.; Williams, L.; Olvera, A.; Zhang, C.; Zhang, M.; Shi, G.; Heron, J. T.; Qi, L.; Guo, L. J.; Kioupakis, E.; Poudeu, P. F. P. Sustainable P-Type Copper Selenide Solar Material with Ultra-Large Absorption Coefficient. *Chemical Science* **2018**, *9* (24), 5405−5414.
(91) Green, M. A.; Dunlop, E. D.; Yoshita, M.; Kopidakis, N.; Bothe, K.; Siefer, G.; Hinken, D.; Rauer, M.; Hohl-Ebinger, J.; Hao, X. Solar Cell Efficiency Tables (Version 64). *Progress in Photovoltaics: Research and Applications* **2024**, *32* (7), 425−441.
(92) Todorov, T.; Gershon, T.; Gunawan, O.; Lee, Y. S.; Sturdevant, C.; Chang, L. Y.; Guha, S. Monolithic Perovskite-CIGS Tandem Solar Cells via in Situ Band Gap Engineering. *Adv. Energy Mater.* **2015**, *5*, 1500799.
(93) Kim, K.; Gwak, J.; Ahn, S. K.; Eo, Y.-J.; Park, J. H.; Cho, J.-S.; Kang, M. G.; Song, H.-E.; Yun, J. H. Simulations of Chalcopyrite/c-Si Tandem Cells Using SCAPS-1D. *Sol. Energy* **2017**, *145*, 52.
(94) Li, X.; Li, J.; Wu, S.; Li, Y.; Peng, C.; Wu, M.; Wu, J.; Lin, J.; Ma, X.; Huang, S. Theoretical Analysis of All-Inorganic Solar Cells Based on Numerical Simulation of CsGeI3/CsPbI3 with p-P+ Built-in Electric Field. *Sol. Energy* **2022**, *247* (2103), 315−329.

https://doi.org/10.1021/acs.langmuir.5c01551
Langmuir 2025, 41, 19729−19741